基于可视中国人蒙特卡罗分析实现肺部无创光学监测的探讨

杨松齐[1]，郭江辉[1,2]，李婷[1*]

¹中国医学科学院北京协和医学院生物医学工程研究所，天津 300192；
²电子科技大学光电科学与工程学院，四川 成都 611731

摘要　肺部疾病的诊断和治疗很重要，目前实现肺部疾病的无创监测具有一定困难。笔者采用近红外光子传输技术，定量研究了人体肺部的结构。以可视中国人数据集（VCH）为实验对象，利用蒙特卡罗（MC）模拟对其进行了仿真。对肺部血流动力学非侵入式测量的可行性进行了理论探讨，并对光子在肺部传输时的最佳光源位置进行了研究，同时还对光源-检测器距离进行了优化。光通量强度显示，光子在人体肺部可以穿透6～8.4 mm，光源到检测器的最佳距离是2.8～3.6 cm。在此基础上，对13名志愿者进行了近红外漫反射实验，实验数据与仿真结果基本一致。实验结果表明，本研究在肺部血流动力学无创监测方面具有广阔的应用前景，同时也为生物医学光学技术在人体上的应用提供了参考。

关键词　医用光学；近红外光谱技术；蒙特卡罗模拟；无创检测；医用光学；肺部监测

中图分类号　TP391.9　　　　**文献标志码**　A　　　　　　　　　　　　**DOI**：10.3788/CJL230532

1　引　　言

肺部疾病是一种有肺部表现的局部或全身性疾病。肺这一器官对于人体的重要性不言而喻，肺部病变或肺部受损会严重影响人体健康。根据世界卫生组织的报告，近年来全球癌症发病率和死亡率呈现持续上升的趋势，其中肺癌位居榜首[1-2]。随着空气污染的加剧、吸烟人口的增加、人口老龄化以及新出现的耐药性病原体[3]，结核病上升为我国第一大传染病，同时尘肺病也占据了职业病的90%[4]。肺部疾病的诊断和治疗十分重要，重症监护室内有很多肺部疾病患者，比如肺癌、重症肺炎、肺气肿、肺动脉栓塞患者，他们都需要无创、持续、即时的监测，因此无创实时肺监测方法对于肺部疾病的预防和治疗具有重要意义。

近红外光谱术（NIRS）已被成功用于监测脑功能活动、休克疾病以及颈部肿瘤的肌肉血流动力学和乳腺情况[5-8]。NIRS可以对多种血流动力学参数进行无创测量，鉴于此，笔者接下来探讨利用近红外光对肺血流动力学进行无创监测的可能性。

人们已利用蒙特卡罗技术模拟了生物细胞中光子传递的性质。Wang[9]开发的MCML（Monte Carlo Modeling of Multi-layered Tissues）软件，是典型的蒙特卡罗仿真方法中应用最多的一款软件。21世纪早期，Bose 等[10]就已经研发出模拟光束在三维非均匀媒质中传播特征的软件。该软件不仅可以设定组织特征，还可以设定入射光的入射方向和极化方向[11]，但操作难度较高。华中科技大学的李婷博士[12]针对目前光学传输模拟技术存在的问题，基于MCML研发了一种新型的蒙特卡罗模拟软件——MCVM（Monte Carlo Modeling of Photon Migration in Voxelized Media）。MCVM 适用于各种尺寸MCML的体素，能够用来描述具有复杂形态和解剖学特征的生物组织。中国数字化可视人体（VCH）中的人体肌肉组织比核磁共振成像（MRI）、电子计算机断层扫描（CT）结果更精确，能够反映肌肉中光的传播特征。包含肺的 VCH 胸部组织被认为是一种最真实的胸部组织模型。此外，在一系列关于光传播研究的蒙特卡罗建模中，MCVM 和 VCH 被成功结合在一起[13]。鉴于此，笔者提出使用 MCVM-VCH 来解决近红外光能否到达并探测到肺的问题。

笔者拟通过 MCVM-VCH 对光传播的建模和 NIRS 实验测量来研究近红外光在所有5个肺叶中的

传播情况。对于 MCVM-VCH 模型，笔者通过静态分析提取了光子传播特性，包括空间灵敏度分布(SSD)、部分路径长度因子(PPF)、差异路径长度因子(DPF)。在每个肺叶上都可以检测到经过传播后到达组织的近红外光信号，这表明无创光学监测肺血流动力学具有巨大潜力。此外，笔者还开发了一种用于肺部的近红外光谱监测系统，并利用该系统进行了预实验，测量了 13 名志愿者肺部的漫射光反射率，定量比较了不同位置的近红外探头在不同肺叶中的测量值。模拟和实验研究结果都表明近红外光无创监测肺血流动力学是一种很有前途的方法，并将支持生物医学光学领域工作者对人类肺部的进一步研究。除了定量研究了近红外光在人体肺部的传输迁移外，笔者还优化了光源-探测器的位置，以便对 5 个不同的肺叶进行无创光学监测。

2　材料和方法

2.1　肺部模型的建立

基于 VCH 数据集进行肺部模型的建立。VCH 数据来自一名成年男性肺部以一定间隔水平切片的切片标本，每片切片都是在组织中可以区分的数字彩色照片，这使得 VCH 能够真实地展现人体的解剖结构[14]。图 1(a)显示了 VCH 模型[15]的原肺部代表性切片。图 1(a)对应的分割图像如图 1(b)所示。在模拟肺部时，将其分为 5 个肺叶区域，如图 1(c)所示。将

200 张这样的图像与图 1(b)结合，用图像处理方法构建三维矩阵，以呈现整个肺组织的结构，如图 1(d)所示。根据肺叶的位置，从图 1(d)中分割出 5 个 420×436×200 体素的肺叶模型。模拟结果也显示了 5 个肺叶的具体情况。每个体素是 0.04 cm×0.04 cm×0.04 cm 的立方体。肺部模型包括皮肤、肌肉、骨骼、脂肪、肝脏、肺、心肌、胃、动脉血和静脉血[16]等 10 种组织类型。

2.2　蒙特卡罗模拟

将蒙特卡罗法用于模拟光在人体肺部的传输迁移。理论上，大量光子进入组织介质后，在运动过程中被介质中的粒子随机散射或吸收。本次研究使用 MCVM 软件，光源设置为 800 nm 点光源。在 800 nm 近红外光波段窗口，10 个组织的光学特性如表 1 所示[17]。μ_a 是吸收系数，μ_s 是散射系数，g 是各向异性因子。光源的初始位置如图 2(a)和图 2(b)所示。不同肺叶对光源位置的要求不同。光源位于胸骨前左第二肋骨附近，为左肺上叶；右肺上叶光源位于胸骨前右第二肋骨附近；右肺中叶光源位于右第四肋骨附近靠近胸骨；左肺下叶光源位于左第八肋骨；右肺下叶光源位于右第八肋骨。模拟时使用了 10^6 个光子，在接下来的数据分析中，进行了 10 次模拟，并计算平均值；然后从 MCVM 软件中获得两个输出文件，分别表示吸收的光子数量和输出光子的分布。
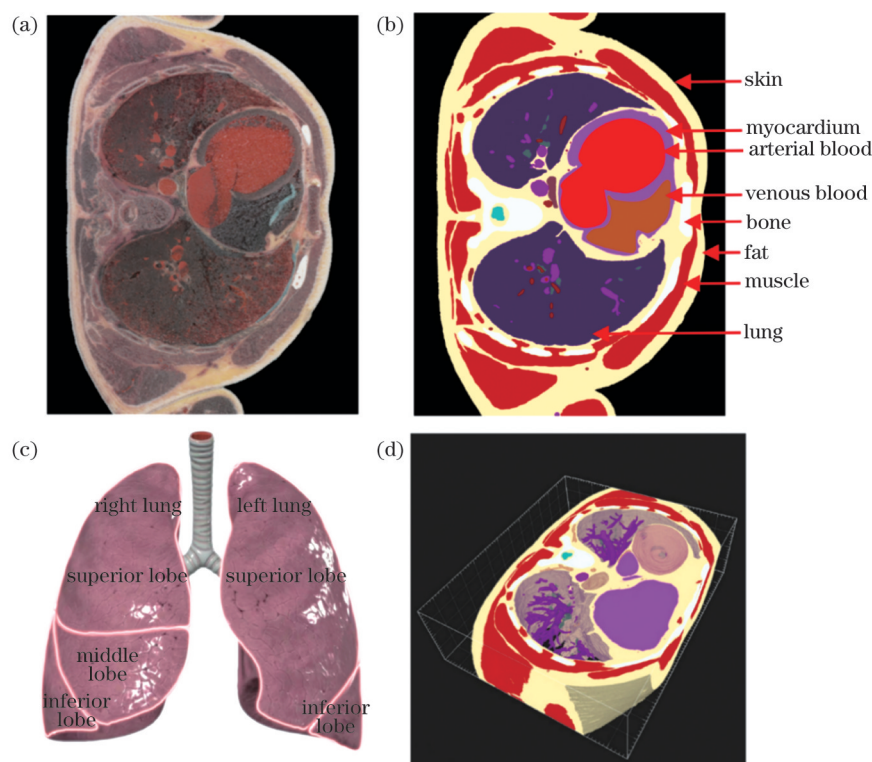

图 1　基于 VCH 的肺部模型。(a)VCH 原肺部图片；(b)在图像(a)中分割组织；(c)5 个肺叶；(d) 3D 图像是 200 张经过处理的图像(b)的排列

Fig. 1　VCH-based lung model. (a) VCH original lung image; (b) segmented tissue from the (a) image; (c) five lung lobes; (d) 3D image is an arrangement of 200 processed (b) images
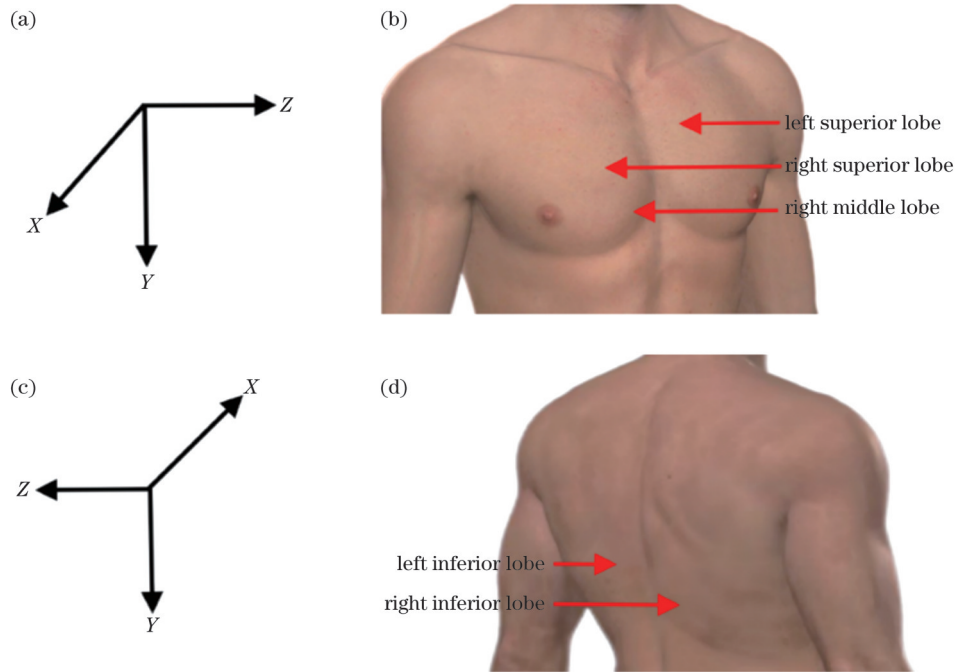
图 2　5个肺叶探测光源的位置。(a)对应图(b)的坐标系;(b)探测左肺上叶、右肺上叶、右肺中叶的光源位置;(c)对应图(d)的坐标系;(b)探测左肺下叶和右肺下叶的光源位置

Fig. 2　Five lung lobes detect light source positions. (a) Coordinate system corresponding to Fig. 2(b); (b) detection of light source positions in the superior lobe of the left lung, the superior lobe of the right lung, and the middle lobe of the right lung; (c) coordinate system corresponding to Fig. 2(d); (d) detection of light source positions in the inferior lobe of the left lung and the inferior lobe of the right lung

表 1　800 nm 波长下组织的光学特性

Table 1　Optical properties of tissues at 800 nm

Tissue type	n	μ_a /cm^{-1}	μ_s /cm^{-1}	g	Reference
Skin	1.37	0.200	73.7	0.715	[18−19]
Muscle	1.40	0.540	66.7	0.930	[20]
Bone	1.43	0.110	291	0.936	[21]
Fat	1.33	0.083	134	0.900	[22]
Liver	1.40	0.800	56.6	0.929	[23]
Lung	1.40	1.000	95.0	0.910	[20]
Myocardium	1.40	0.920	103	0.930	[24−25]
Stomach	1.40	0.780	47.0	0.761	[26]
Arterial blood	1.40	2.333	522	0.990	[27−28]
Venous blood	1.40	2.338	440	0.990	[27−28]

2.3　空间灵敏度分布

空间灵敏度分布(SSD,在公式中记为"S_{SD}")是指检测光对组织中不同位置光强度变化的敏感程度分布,它描述了光在组织中的传播路径对光强度变化的响应情况。文献[29]中介绍了计算函数。简言之,利用式(1)计算 SSD[30]。

$$S_{SD}(\boldsymbol{r}_S, \boldsymbol{r}_D, \boldsymbol{r}_m) = F(\boldsymbol{r}_S, \boldsymbol{r}_m) \times F(\boldsymbol{r}_D, \boldsymbol{r}_m), \quad (1)$$

其中,

$$F(\boldsymbol{r}_X, \boldsymbol{r}_m) = \frac{A(\boldsymbol{r}_X, \boldsymbol{r}_m)}{\mu_a(\boldsymbol{r}_m)}, \quad (2)$$

式中:$F(\boldsymbol{r}_S, \boldsymbol{r}_m)$表示从第 m 个体素到光源的信号量;

$F(\boldsymbol{r}_D, \boldsymbol{r}_m)$ 表示从第 m 个体素到探测器的信号量;$F(\boldsymbol{r}_S, \boldsymbol{r}_m)$ 和 $F(\boldsymbol{r}_D, \boldsymbol{r}_m)$ 由式(2)计算;$A(\boldsymbol{r}_X, \boldsymbol{r}_m)$ 表示体素 $\boldsymbol{r}_m$ 在 $\boldsymbol{r}_X$ 上的吸收,来自吸收的光子文件;$\mu_a(\boldsymbol{r}_m)$ 表示体素 $\boldsymbol{r}_m$ 的吸光度。

2.4　实验设计

笔者设计了一个实验,旨在研究探测到的肺部光强信号。本课题组[31]研制了一种基于近红外技术的设备。类似的近红外器件性能的可靠性和稳定性已经得到证明[32−33]。该装置由 3 个模块组成:近红外探测器、控制和处理模块以及数据采集应用程序。探头以 800 nm LED(AlGaAs 材料)为光源,以 OPT101 为光电传感器。800 nm LED 与近红外探测器的间距为 2.8 cm。这种间隔对于大多数肺叶来说是最好的光源-探测器距离(L_{SD})。探测器由一块灵活的电路板组装而成,它能更好地附着在皮肤上,并且较少受到环境光的干扰。控制和处理模块从探头中获取信号,并通过蓝牙将其发送至移动应用程序。

在初步实验研究中,测量了 13 名年轻健康志愿者肺部的光强信号。13 名志愿者中包括 4 名女性和 9 名男性,年龄集中在 25~35 岁之间。在实验过程中,光源依次放置在 5 个肺叶对应的位置(如图 3 所示)。志愿者的前胸检测到三个位置的光强度,如图 3(a)所示;志愿者的背部检测到两个位置的光强度,如图 3(b)所示。测量前要求所有受试者安静躺下休息 2~3 min,使呼吸稳定。采集指令由手机应用程序发
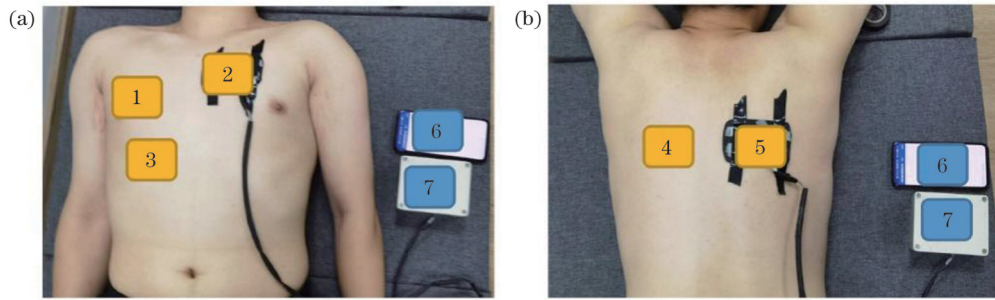
图 3 肺部光强信号的初步实验。1～5 分别表示右肺上叶、左肺上叶、右肺中叶、左肺下叶、右肺下叶的位置，6 表示手机应用程序（上位机），7 表示近红外探测设备。(a)探测志愿者 1、2、3 位置的光信号；(b)探测志愿者 4、5 位置的光信号

Fig. 3 Preliminary experiments of light intensity signals in the lungs. Digits 1–5 indicate the positions of the superior lobe of the right lung, the superior lobe of the left lung, the middle lobe of the right lung, the inferior lobe of the left lung, and the inferior lobe of the right lung, respectively. Digit 6 indicates the cell phone application (upper computer). Digit 7 indicates the NIR detection device. (a) Detection of light signals at positions 1, 2, and 3 of volunteers; (b) detection of light signals at positions 4 and 5 of volunteers

出，主要指令是光源的波长和采集频率，这些指令通过蓝牙传输到近红外设备，然后由近红外装置采集各个位置的光强信号，收集数据时间为 2 min。

3 分析与讨论

3.1 肺部 SSD

使用前文提到的 VCH 肺部模型，通过 MCVM 软件进行蒙特卡罗仿真模拟计算来获得肺的 SSD。根据式(1)和式(2)计算 5 个肺叶的 SSD，得出左肺下叶的 SSD 为 0.0235%，左肺上叶的 SSD 为 0.0252%，右肺下叶的 SSD 为 0.0368%，右肺中叶的 SSD 为 0.0348%，右肺上叶的 SSD 为 0.0270%。光子进入肺部之前会通过 4 种组织，即皮肤、脂肪、肌肉和骨骼。由于脂肪的分布不同，光子通过脂肪组织到达各部分肺叶的时间不同[34]。在光子从皮肤表面向目标组织传播过程中，光强是逐渐衰减的。具体来说，当光源从右背向右肺下叶发射光子时，光子的穿透深度为 36 mm，如图 4(a)所示；当光源从左胸进入左肺上叶时，光子的
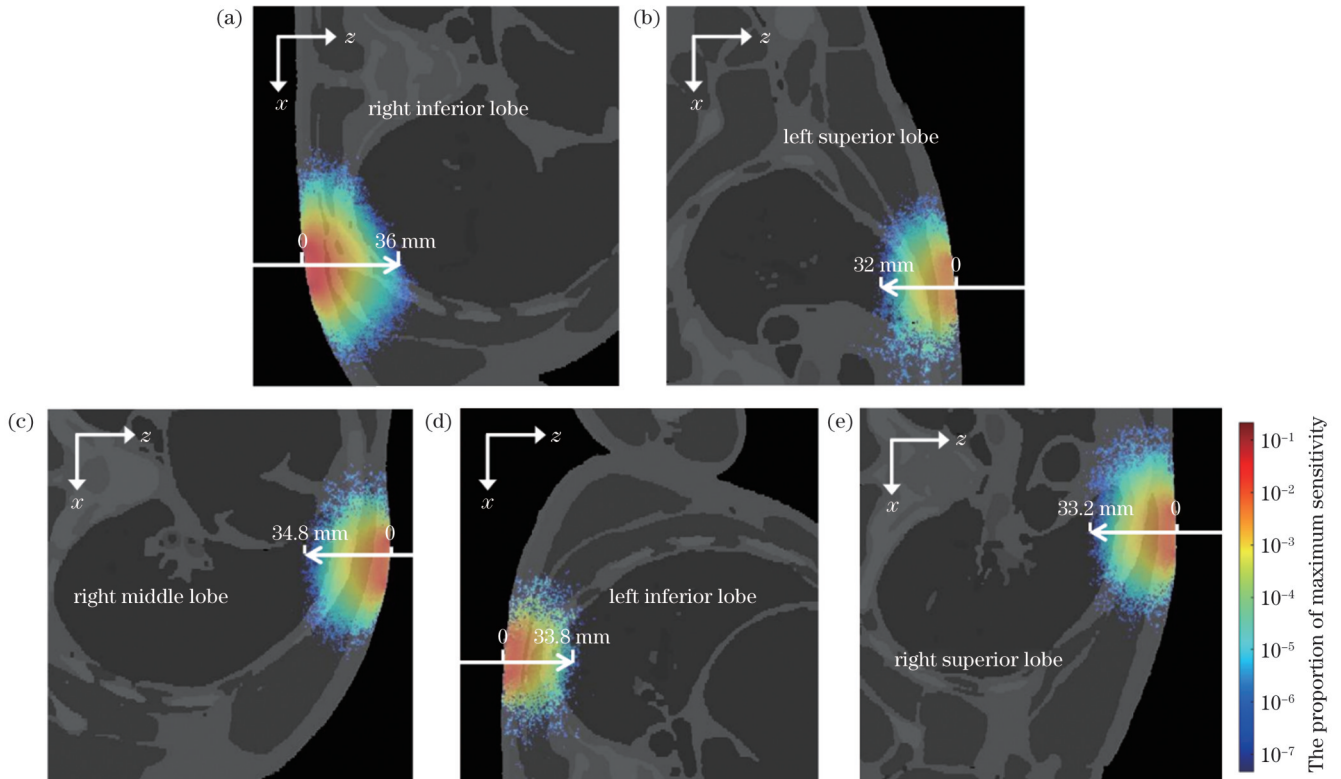

图 4 5 个肺叶的光通量分布图像。(a)右肺下叶；(b)左肺上叶；(c)右肺中叶；(d)左肺下叶；(e)右肺上叶。"0"点和箭头分别表示光源的起点和光子发射方向

Fig. 4 Light fluence distribution images of the five lung lobes. (a) Inferior lobe of the right lung; (b) superior lobe of the left lung; (c) middle lobe of the right lung; (d) inferior lobe of the left lung; (e) superior lobe of the right lung. The dot "0" and arrow indicate the starting point of the light source and the direction of photon emission, respectively

穿透深度约为 32 mm,如图 4(b)所示;当光源从右胸腔向右肺中叶发射光子时,光子的穿透深度为 34.8 mm,如图 4(c)所示;当光源从左背向左肺下叶发射光子时,光子的穿透深度为 33.8 mm,如图 4(d)所示;当光源从右胸腔向右肺上叶发射光子时,光子的穿透深度为 33.2 mm,如图 4(e)所示。一般来说,800 nm 波长的光子在人体内的穿透深度可达 32~36 mm,在肺部的穿透距离可达到 6~8.4 mm。到达肺部的光通量与皮肤表面的光通量强度相比急剧下降,约下降为后者的 $1/10^5$。虽然到达肺部的光通量强度很低,但仍然可以准确地检测到它,说明非侵入性光学监测是可行的。

3.2 光子吸收

人体组织会与光产生交互作用,包括透射、散射、折射、反射、吸收等[35],大多数光子在人体传播过程中都会被组织介质吸收。本文通过研究肺叶中的光子吸收(如图 5 所示),得出左肺下叶的光子吸收率为 6%~8%,左肺上叶的光子吸收率为 7%~8%。左肺叶的光子吸收率随光源-探测器距离 L_{SD} 的变化而改变。当光源-探测器距离 L_{SD} 为 2.5 cm 时,左肺两叶的光子吸收率达到最大值。右肺下叶的光子吸收率为 9.5%~11%,当光源-探测器距离 L_{SD} 为 2 cm 时,吸收率最大。右肺中叶的光子吸收率为 8%~9.5%,当光源-探测器距离 L_{SD} 为 2.5 cm 时,达到最大光子吸收率。右肺上叶的光子吸收率为 7.8%~8.2%,当光源-探测器距离 L_{SD} 为 3 cm 时,吸收最大。综上所述,肺的平均光子吸收率约为 9%。在达到最大光子吸收率后,随着光源-探测器距离 L_{SD} 增加,光子吸收率减小。
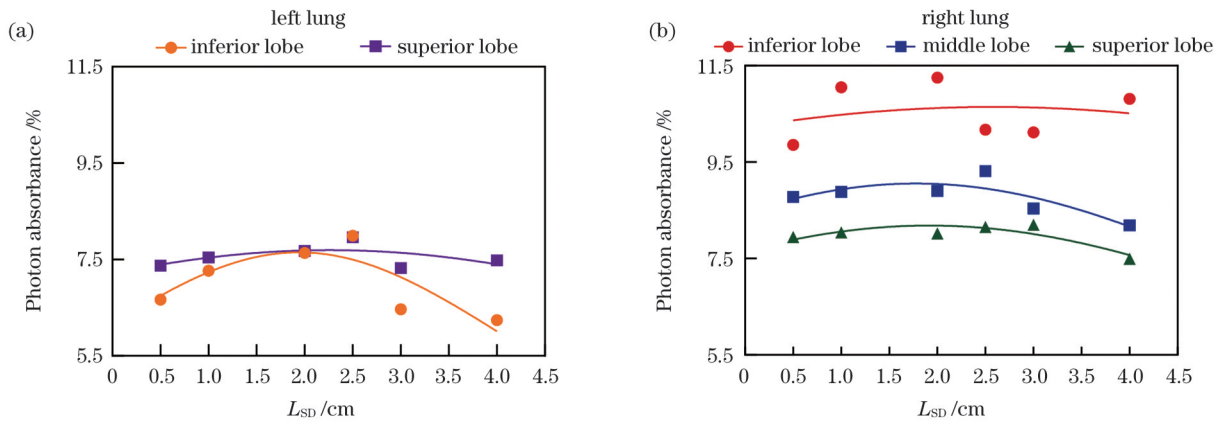

图 5 5个肺叶的光子吸收率随光源-探测器距离 L_{SD} 的变化。(a)左肺叶光子吸收率随 L_{SD} 的变化;(b)右肺叶光子吸收率随 L_{SD} 的变化

Fig. 5 Changes in photon absorbance of the five lung lobes with source-detector distance L_{SD}. (a) Photon absorbance of the left lung lobe changes with L_{SD}; (b) photon absorbance of the right lung lobe changes with L_{SD}

3.3 光源-探测器距离优化

接下来对光源-探测器距离进行优化。随着光源-探测器距离改变,DPF、PPF 的值也会发生变化。DPF 是将源-探测器分离度与光的平均路径长度联系起来的比例系数,由 DPF 的概念可知着色团的变化对采样区域是全局性的[9]。PPF 也是一个类似的比例因子,但它假设焦点发生变化。因此,PPF 代表了一个比例因子,它将源-探测器距离转化成光通过色团变化的焦点区域的平均路径长度[36-38]。因此,通过比较这些值的变化,可以找到最优的光源-探测器距离。计算了5个肺叶的 DPF、PPF 随光源-探测器距离的变化,计算结果如图 6 所示。对 DPF 与光源-探测器距离 L_{SD} 进行非线性回归拟合后可以得出,随着光源-探测器距离 L_{SD} 的增加,5个肺叶的 DPF 呈增长趋势,如图 6(a1)~(a5)所示。左肺下叶的 PPF 在光源-探测器距离 L_{SD} 为 3.4 cm 时达到峰值,然后迅速下降,如图 6(b1)所示。左肺上叶的 PPF 在光源-探测器距离 L_{SD} 为 3.6 cm 时达到峰值,然后迅速下降,如图 6(b2)所示。右肺下叶的 PPF 在光源-探测器距离 L_{SD} 为 3.1 cm 时达到峰值,然后急剧下降,如图 6(b3)所示。右肺中叶的

PPF 在光源-探测器距离 L_{SD} 为 3.3 cm 时达到峰值,然后急剧下降,如图 6(b4)所示。右肺上叶的 PPF 在光源-探测器距离 L_{SD} 为 2.9 cm 处有一个峰值,当 L_{SD} 大于该值时,PPF 显著下降,如图 6(b5)所示。总体而言,5个肺叶的 PPF 指数反映了光强信号对肺部的敏感性,随着光源-探测器距离 L_{SD} 增加,PPF 指数呈现出先增大后减小的趋势。结合 DPF 以及 PPF 指数分析可以得出,5个肺叶对应的最佳光源-探测器距离 L_{SD} 的范围为:左肺下叶 3.3~3.5 cm,左肺上叶 3.5~3.6 cm,右肺下叶 3.0~3.1 cm,右肺中叶 3.3~3.4 cm,右肺上叶 2.8~2.9 cm。

3.4 实验结果

对实验中采集的 13 名健康志愿者肺部的光强信号进行处理。一方面,对实验中获得的5个位置的光强信号进行滤波,以消除部分干扰的影响;然后计算出每个志愿者对应肺叶位置光强信号的中位数,以此来表示该志愿者肺叶中的光强信号。另一方面,用模拟的5个肺叶的光子吸收率表示每个肺叶的光强度。在这里,选择与实验相同的光源-探测器距离 L_{SD} 下的光子吸收率。选取 13 名志愿者肺部的光强中位数,并将
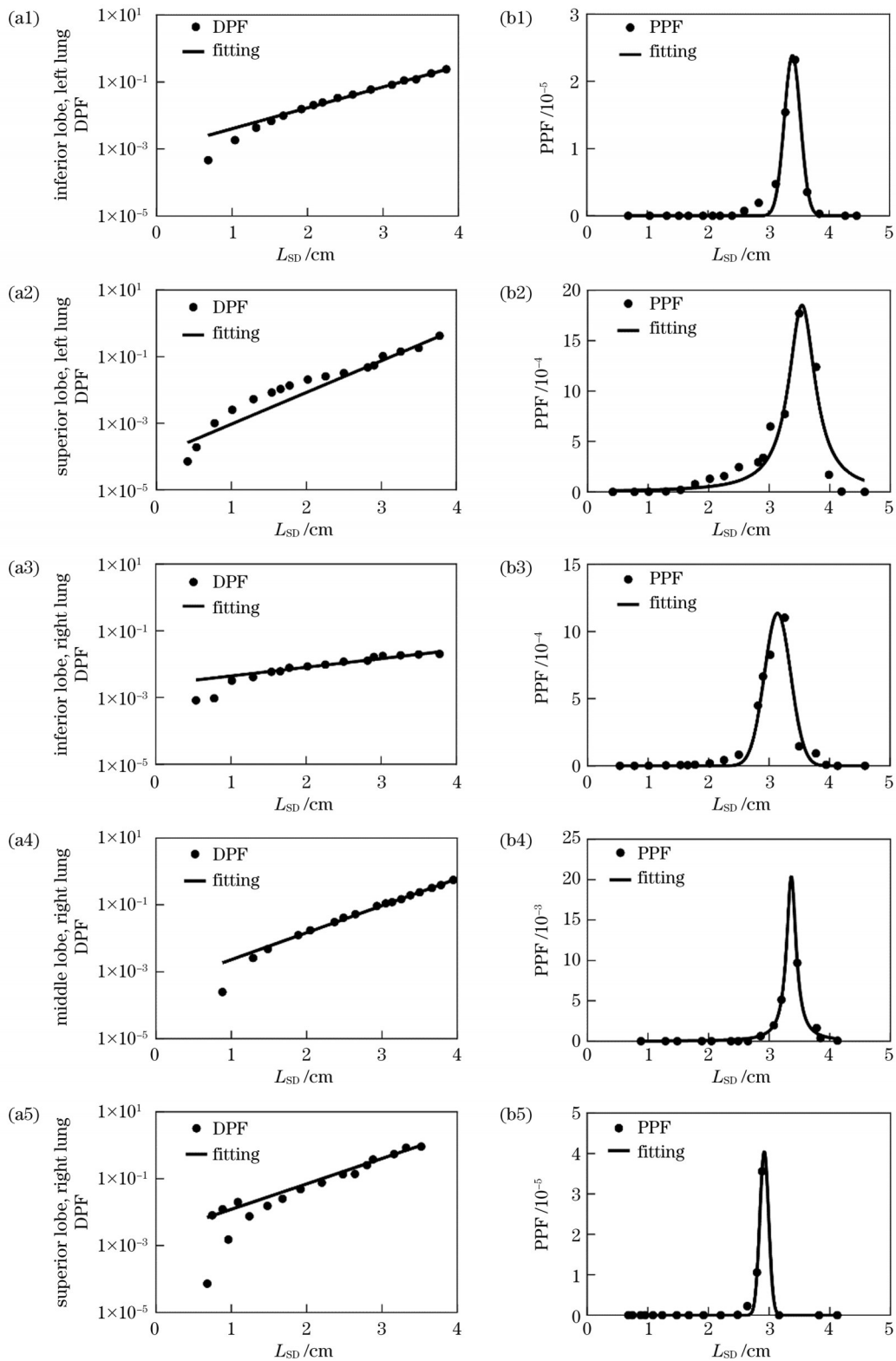
图 6　5 个肺叶的 DPF 和 PPF 关于光源-探测器距离 L_{SD} 的函数图。(a1)(b1)左肺下叶；(a2)(b2)左肺上叶；(a3)(b3)右肺下叶；
(a4)(b4)右肺中叶；(a5)(b5)右肺上叶

Fig. 6　DPF and PPF as a function of source-detector distance L_{SD} for the five lung lobes. (a1)(b1) Inferior lobe of the left lung;
(a2)(b2) superior lobe of the left lung; (a3)(b3) inferior lobe of the right lung; (a4)(b4) middle lobe of the right lung;
(a5)(b5) superior lobe of the right lung

其与模拟值进行比较。可以看出，两者具有相似的趋势，如图 7(a)所示。实验值和模拟值也有很强的相关性，$P < 0.05$，如图 7(b)所示。接下来，将实验中一名男性志愿者 5 个肺叶的光强与模拟的光强进行比较。实验值均小于模拟值，如图 7(c)所示，但实验值与模拟值有很大的相关性，$P < 0.05$，如图 7(d)所示。
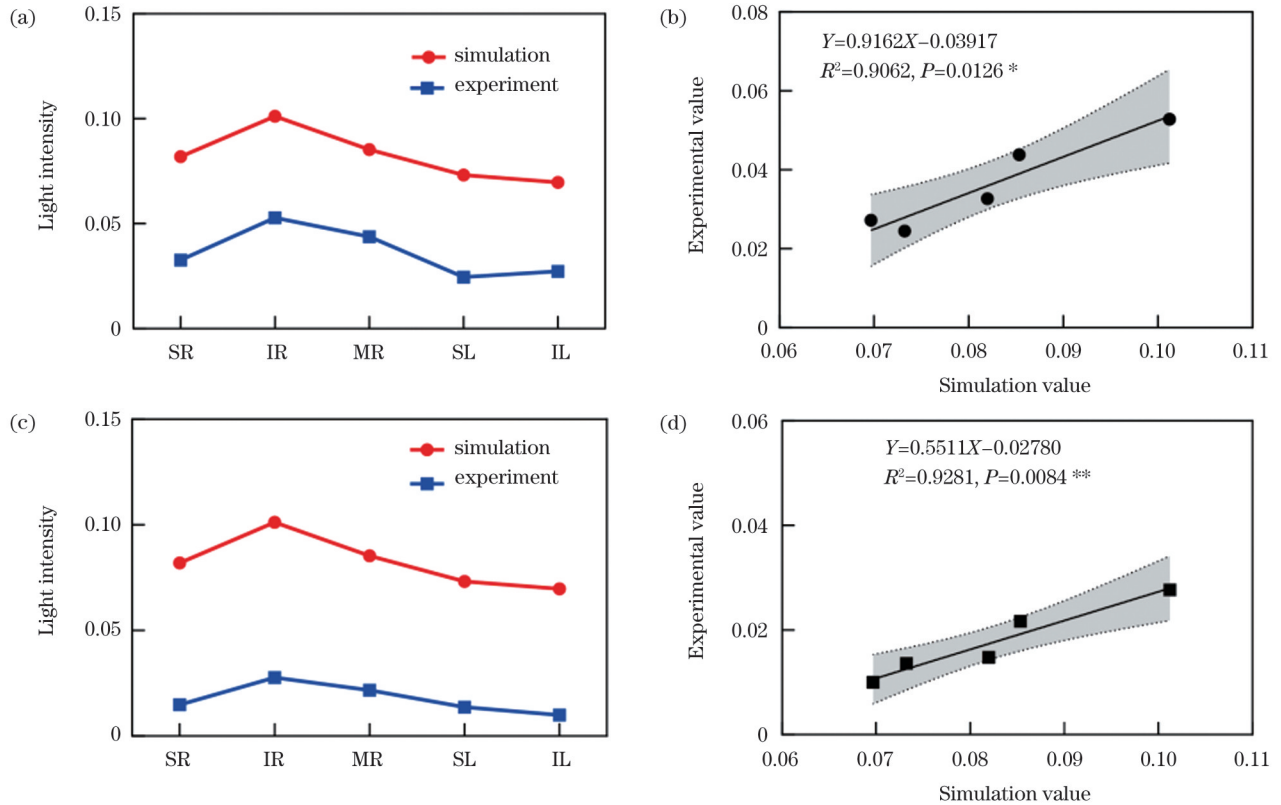
图 7　肺部探测区域实验光强和模拟光强的比较。(a) 13 名志愿者每个肺叶光强实验值与模拟值的比较，其中 SR 代表右肺上叶，IR 代表右肺下叶，MR 代表右肺中叶，SL 代表左肺上叶，IL 代表左肺下叶；(b)图像(a)中实验值与模拟值的拟合，其中 R^2 为决定系数，*代表 $P<0.05$，**代表 $P<0.01$；(c)一名男性志愿者 5 个肺叶的光强实验值与模拟值的比较；(d)图像(c)中实验值与模拟值的拟合

Fig. 7　Comparison of experimental and simulated light intensities in the lung detection region. (a) Comparison of experimental and simulated light intensities in each lung lobe of 13 volunteers, where "SR" represents superior lobe of the right lung, "IR" represents inferior lobe of the right lung, "MR" represents middle lobe of the right lung, "SL" represents superior lobe of the left lung, and "IL" represents inferior lobe of the left lung; (b) fitting of experimental and simulated values in Fig. 7(a), where R^2 is the coefficient of determination, * represents $P<0.05$ and ** represents $P<0.01$; (c) comparison of experimental and simulated light intensities in 5 lung lobes of a male volunteer; (d) fitting of experimental and simulated values in Fig. 7(c)

4　结　论

在 VCH 肺部模型的基础上，采用近红外光谱技术和蒙特卡罗模拟方法定量分析了人体肺部的光子迁移特性。肺部的光通量分布和光通量强度的变化表明，光子从光源发射经过传输可以迁移到肺部。光子从皮肤到肺的穿透深度为 32～36 mm，其中肺内的光子穿透深度为 6～8.4 mm，5 个肺叶的 SSD 为 0.0235%～0.0368%。此外，在肺部光强实验中得出的肺部探测的最佳光源-探测器距离 L_{SD} 为 2.8～3.6 cm。为了保证获得更好的光强信号，应在最佳 L_{SD} 范围内进行探测。实验数据显示，计算的光强值远远小于模拟的光强值，如图 7(a)和图 7(c)所示，但仍在可检测的范围内。从 5 个肺叶的总体光强趋势来看，实验值与模拟值之间存在相关性，$P<0.05$，如图 7(b)和图 7(d)所示。这表明，在 5 个位置检测到的光强信号可能来自 5 个肺叶，从而进一步证明了人体肺部无创光学监测的可行性。

本研究还可为功能性近红外光谱人体肺部监测提供理论支持，同时为优化光源-探测器距离 L_{SD} 提供了途径，希望本研究能对生物医学光学领域的肺部疾病研究起到抛砖引玉的作用。

参 考 文 献

[1] World Health Organization. Assessing national capacity for the prevention and control of noncommunicable diseases: report of the 2019 global survey[R]. Geneva: World Health Organization, 2020.

[2] Ferlay J, Ervik M, Lam F, et al. Global cancer observatory: cancer today[EB/OL]. [2023-02-03]. https://gco.iarc.fr/today.

[3] Sun H, Zhang L J, Sui B W, et al. The effect of terpenoid natural Chinese medicine molecular compound on lung cancer treatment[J]. Evidence-Based Complementary and Alternative Medicine, 2021, 2021: 3730963.

[4] Zhou M G, Wang H D, Zeng X Y, et al. Mortality, morbidity, and risk factors in China and its provinces, 1990-2017: a systematic analysis for the Global Burden of Disease Study 2017[J]. The Lancet, 2019, 394(10204): 1145-1158.

[5] Fukui Y, Ajichi Y, Okada E. Monte Carlo prediction of near-infrared light propagation in realistic adult and neonatal head models [J]. Applied Optics, 2003, 42(16): 2881-2887.

[6] Li T, Li Y, Sun Y L, et al. Effect of head model on Monte Carlo modeling of spatial sensitivity distribution for functional near-infrared spectroscopy[J]. Journal of Innovative Optical Health Sciences, 2015, 8(5): 1550024.

[7] Pan B A, Huang C, Fang X, et al. Noninvasive and sensitive optical assessment of brain death[J]. Journal of Biophotonics, 2019, 12(3): e201800240.

[8] Nioka S, Shnall M, Conant E, et al. Breast cancer detection of large size to DCIS by hypoxia and angiogenesis using NIRS[C]// Huffel S, Naulaers G, Caicedo A, et al. Oxygen transport to tissue XXXV. Advances in experimental medicine and biology. New York: Springer, 2013, 789: 211-219.

[9] Wang L H. Monte Carlo modeling of photon transport in multi-layered tissues[J]. Computer Methods and Programs in Biomedicine, 1995, 4: 131-146.

[10] Boas D A, Dale A M. Simulation study of magnetic resonance imaging-guided cortically constrained diffuse optical tomography of human brain function[J]. Applied Optics, 2005, 44(10): 1957-1968.

[11] Zhu C G, Liu Q. Review of Monte Carlo modeling of light transport in tissues[J]. Journal of Biomedical Optics, 2013, 18(5): 050902.

[12] 李婷. 光在三维结构组织中传输的 MC 模拟及脑功能成像研究 [D]. 武汉: 华中科技大学, 2010.
Li T. Study on MC simulation and brain functional imaging of light transmission in three-dimensional structure tissue[D]. Wuhan: Huazhong University of Science and Technology, 2010.

[13] 王安乐, 李婷, 邓勇, 等. 基于 MCVM 研究真实前臂结构对光传输的影响[J]. 光学学报, 2011, 31(3): 0317002.
Wang A L, Li T, Deng Y, et al. Influence of real forearm structure on light transport based on MCVM[J]. Acta Optica Sinica, 2011, 31(3): 0317002.

[14] Li T, Gong H, Luo Q M. Visualization of light propagation in visible Chinese human head for functional near-infrared spectroscopy[J]. Journal of Biomedical Optics, 2011, 16(4): 045001.

[15] Takatani S, Graham M D. Theoretical analysis of diffuse reflectance from a two-layer tissue model[J]. IEEE Transactions on Bio-Medical Engineering, 1979, 26(12): 656-664.

[16] Li T, Lin Y, Shang Y, et al. Simultaneous measurement of deep tissue blood flow and oxygenation using noncontact diffuse correlation spectroscopy flow-oximeter[J]. Scientific Reports, 2013, 3: 1358.

[17] Jacques S L. Optical properties of biological tissues: a review[J]. Physics in Medicine and Biology, 2013, 58(11): R37-R61.

[18] Yan S J, Jacques S L, Ramella-Roman J C, et al. Graphics-processing-unit-accelerated Monte Carlo simulation of polarized light in complex three-dimensional media[J]. Journal of Biomedical Optics, 2022, 27(8): 083015.

[19] Li P C, Liu C L, Li X P, et al. GPU acceleration of Monte Carlo simulations for polarized photon scattering in anisotropic turbid media[J]. Applied Optics, 2016, 55(27): 7468-7476.

[20] Oulhaj H, Wojak J, Tricoli U, et al. Diffuse optical tomography with polarized light: a GPU-accelerated polarization-sensitive Monte Carlo simulations for efficient sensitivity kernel computation [C]//European Conference on Biomedical Optics 2019, June 23-25, 2019, Munich, Germany. Washington D.C: Optica Publishing Group, 2019: 11074_30.

[21] Doronin A, Meglinski I. The application of a unified Monte Carlo model in the training of artificial neural networks for the purpose of real-time *in-vivo* sensing of tissue optical properties[J]. Proceedings

of SPIE, 2019, 10982: 109820N.

[22] Doronin A, Meglinski I. Online object oriented Monte Carlo computational tool for the needs of biomedical optics[J]. Biomedical Optics Express, 2011, 2(9): 2461-2469.

[23] Doronin A, Meglinski I. Peer-to-peer Monte Carlo simulation of photon migration in topical applications of biomedical optics[J]. Journal of Biomedical Optics, 2012, 17(9): 090504.

[24] Fang Q Q, Yan S J. MCX cloud: a modern, scalable, high-performance and in-browser Monte Carlo simulation platform with cloud computing[J]. Journal of Biomedical Optics, 2022, 27(8): 083008.

[25] Berrocal E, Sedarsky D L, Paciaroni M E, et al. Laser light scattering in turbid media Part I: experimental and simulated results for the spatial intensity distribution[J]. Optics Express, 2007, 15 (17): 10649-10665.

[26] Berrocal E, Sedarsky D L, Paciaroni M E, et al. Laser light scattering in turbid media Part II: spatial and temporal analysis of individual scattering orders via Monte Carlo simulation[J]. Optics Express, 2009, 17(16): 13792-13809.

[27] Frantz D, Jönsson J, Berrocal E. Multi-scattering software Part II: experimental validation for the light intensity distribution[J]. Optics Express, 2022, 30(2): 1261-1279.

[28] Jönsson J, Berrocal E. Multi-scattering software Part I: online accelerated Monte Carlo simulation of light transport through scattering media[J]. Optics Express, 2020, 28(25): 37612-37638.

[29] Meglinskiĭ I V, Matcher S D. Analysis of the spatial distribution of detector sensitivity in a multilayer randomly inhomogeneous medium with strong light scattering and absorption by the Monte Carlo method[J]. Optics and Spectroscopy, 2001, 91(4): 654-659.

[30] Li T, Duan M X, Li K, et al. Bedside monitoring of patients with shock using a portable spatially-resolved near-infrared spectroscopy [J]. Biomedical Optics Express, 2015, 6(9): 3431-3436.

[31] Li T, Li Z B, Zhao K, et al. Reliability analysis of a mini-instrument for simultaneous monitoring water content, deep tissue temperature, and hemodynamic parameters[J]. Microelectronics Reliability, 2018, 86: 72-76.

[32] Li T, Su Y, Wu L H, et al. Reliability analysis of a newly developed detector for monitoring spine health[J]. Microelectronics Reliability, 2017, 78: 411-414.

[33] Zhao Y, Xu G Y, Sun Y L, et al. A portable high-density absolute-measure NIRS imager for detecting prefrontal lobe activity under fatigue driving[J]. Microelectronics Reliability, 2018, 82: 197-203.

[34] Bykov A, Tuchin V, Meglinski I. Multiplexed spatially-focused localization of light in adipose biological tissues[J]. Scientific Reports, 2022, 12: 9711.

[35] 李婷. 生物医学光子传输[M]. 武汉: 武汉大学出版社, 2015.
Li T. Biomedical photon transmission[M]. Wuhan: Wuhan University Press, 2015.

[36] Arridge S R, Schweiger M, Hiraoka M, et al. A finite element approach for modeling photon transport in tissue[J]. Medical physics, 1993, 20(2): 299-309.

[37] Strangman G, Franceschini M A, Boas D A. Factors affecting the accuracy of near-infrared spectroscopy concentration calculations for focal changes in oxygenation parameters[J]. NeuroImage, 2003, 18(4): 865-879.

[38] Steinbrink J, Wabnitz H, Obrig H, et al. Determining changes in NIR absorption using a layered model of the human head[J]. Physics in Medicine and Biology, 2001, 46(3): 879-896.

Noninvasive Optical Monitoring of Lung Based on Monte Carlo Analysis of Visual Chinese Human

Yang Songqi[1]，Guo Jianghui[1,2]，Li Ting[1*]

[1]*Institute of Biomedical Engineering, Chinese Academy of Medical Sciences & Peking Union Medical College, Tianjin 300192, China;*

[2]*School of Optoelectronic Science and Engineering, University of Electronic Science & Technology of China, Chengdu 611731, Sichuan, China*

Abstract

Objective　Lung disease is a local or systemic disease characterized by pulmonary manifestations. The importance of this organ，the lung，to the human body cannot be overstated，and a diseased or damaged lung can seriously affect human health. According to the World Health Organization，global cancer incidence and mortality rates have shown a continuous increase in recent years，with lung cancer topping the list. With increasing air pollution，a growing smoking and aging population，and the emergence of drug-resistant pathogens，tuberculosis and pneumoconiosis have become the top two infectious diseases in China，accounting for 90％ of occupational disease cases. The diagnosis and treatment of lung diseases are becoming increasingly important，and many patients with lung diseases such as lung cancer，severe pneumonia，emphysema，and pulmonary embolism in intensive care units require noninvasive，continuous，and immediate monitoring. Thus，noninvasive real-time lung monitoring methods are important for the prevention and treatment of lung diseases.

Methods　The VCH slice specimens used in this study were from an adult male that was sliced horizontally at regular intervals in a standing position. Each slice was a digital color photograph with distinguishable tissues. The lung was divided into five lobe regions for simulations. Two hundred such images were combined with image processing methods to construct a three-dimensional matrix to present the entire lung tissue structure. According to the location of the lung lobes，five lung lobe models of 420 voxel×436 voxel× 200 voxel were segmented. The simulation results showed the specific situation of the five lung lobes. Each voxel was a 0.04 cm× 0.04 cm×0.04 cm cube. The Monte Carlo method was used to simulate the migration of light in the lungs. This study used the MCVM software，which targets 3D voxelized media. In the simulation，the light source was set to an 800 nm point light source，and the optical properties of 10 tissues were in the near-infrared band at 800 nm. The light source was initially located near the fourth right rib near the sternum body. Additionally，in a preliminary experiment，light intensity signals were measured in the lungs of 13 young healthy volunteers. The 13 volunteers included 4 women and 9 men (25–35 years old). During the experiment，the light sources were placed at the corresponding positions of the five lung lobes in turn. The volunteers' prothorax detected light intensity at three locations. The back of the volunteer detected light intensity at two locations. All subjects were asked to lie down quietly and rest for 2–3 min before the measurements to allow their breathing to stabilize. The parameters for the experiment were set based on near-infrared device applications. The main parameters are the wavelength of the light source and the collection frequency. These parameters were transmitted to the near-infrared device using bluetooth. Then，the light intensity signals at each position were collected by the near-infrared device. The parameters collection time was 2 min.

Results and Discussions　Based on the VCH lung model (Fig. 1)，this study used the Monte Carlo simulation method to quantitatively analyze the photon migration characteristics in the human lung. The light fluence distribution in the lungs and the changes in the light fluence intensity indicated that photons could reach the lungs from the light source (Fig. 3). The photon penetration depth from the skin to the lung was 32–36 mm，while the photon penetration depth in the lung was 6–8.4 mm. The SSD for the five lobes was 0.0235％–0.0368％. The average photon absorption of five lung lobes was approximately 9％ (Fig. 4). The differences in photon migration in the five lung lobes could be reflected. Additionally，we proposed an optimization plan for the source-detector distance (L_{SD}). According to the two path length factors，PPF and DPF，combined with the PPF/DPF index，the L_{SD} in the lungs could be the optimal topological location between 2.8 and 3.6 cm；however，the distance from the superior lobe of the right lung was 3.3–3.5 cm. Using VCH-based Monte Carlo simulations of human lungs，the optical migration characteristics of the lungs were quantitatively visualized，the feasibility of noninvasive optical detection of the lungs was proven，and the optimal L_{SD} for the optical detection of the lungs was found. This study performed optimization to determine the important parameter L_{SD} for optical noninvasive testing of the lungs. The optimal lung L_{SD} was 2.8–3.6 cm，but the optimal spacing of the superior lobe of the right lung was 3.3–3.5 cm. Compared to previous studies on the detection of other parts of the human body in the biomedical optics community，the optimal distance between the lungs was significantly smaller than the optimal distance in other body parts. The optimal spacing for these different body parts has been reported to be approximately 3 cm. In this case，a greater separation distance did not a better result. On the contrary，with an increase in the spacing of the source-detector，the energy density of the transmitted photon rapidly decreased，which seriously affected the quality of the detection signal. The optimal separation preference depended on the detection of light density and the path length factors，PPF and DPF. In a preliminary lung light intensity experiment，the L_{SD} spacing was 2.8 cm，

which was within the optimal L_{SD} range for the lung. A better light intensity signal could be obtained by performing detection in the optimal L_{SD} range. The experimental data showed that the light intensity values calculated from the detection were much smaller than the simulated light intensity values [Fig. 7(a) and Fig. 7(c)]. The overall light intensity trend of the five locations indicated a correlation between the experimental and simulated values with $P<0.05$ [Fig. 7(b) and Fig. 7(d)]. This implied that the detected light intensity signals at the five locations may come from five lung lobes. This further proves the feasibility of the noninvasive optical detection of human lungs.

Conclusions In summary, this study used Monte Carlo simulations to visualize the propagation of near-infrared light in a VCH lung model. Photon migration in the lungs was studied. Photon absorption of each lobe was shown to be approximately 9%. The optimal source-detector distance in the superior lobe of the right lung was found to be 2.8−2.9 cm, while the optimal distance for the other lung lobes was 3.0−3.6 cm. A preliminary experiment demonstrated the feasibility of optical detection of the lungs. This study also provided theoretical support for using functional near-infrared spectroscopy for lung detection and a reference for the optimal L_{SD}. It is hoped that the results of this study will promote research on lung diseases in the biomedical optics community.

Key words medical optics; near-infrared spectroscopy; Monte Carlo simulation; non-invasive detection; medical optics; lung monitoring